One-step Polyol Synthesis and Langmuir−Blodgett Monolayer Formation of Size-tunable Monodisperse Rhodium Nanocrystals with Catalytically Active (111) Surface Structures

Yawen Zhang,[†,‡] Michael E. Grass,[†] Susan E. Habas,[†] Feng Tao,[†] Tianfu Zhang,[†] Peidong Yang,[†] and Gabor A. Somorjai*[,†]

Department of Chemistry, University of California, Berkeley, California 94720, Chemical and Materials Sciences Divisions, Lawrence Berkeley National Laboratory, 1 Cyclotron Road, Berkeley, California 94720, College of Chemistry and Molecular Engineering and State Key Lab of Rare Earth Materials Chemistry and Applications and PKU−HKU Joint Lab in Rare Earth Materials and Bioinorganic Chemistry, Peking University, Beijing 100871, China

Received: May 2, 2007; In Final Form: June 22, 2007

Size-tunable monodisperse Rh nanocrystals can offer unique properties for many heterogeneous catalytic reactions (such as hydrogenation, hydroformylation, and hydrocarbonylation) of both scientific and technological interest. In this article, we report the synthesis of monodisperse, well-shaped Rh nanocrystals in a range of 5−15 nm by a one-step polyol reduction at temperatures of 170−230 °C under Ar, using rhodium(III) acetylacetonate [$Rh(acac)_3$] as the source of metal ions, 1,4-butanediol as the reducing solvent, and poly(vinylpyrrolidone) as the capping agent. Two-dimensional projects of the nanocrystals are polygons, dominated by hexagons, pentagons, and triangles with catalytically active (111) surfaces (>65% yield). Over 45% of the polygons are multiple (111) twinned particles (hexagons and pentagons), favored by thermodynamics. To achieve size uniformity, adjustment of the reduction kinetics of $Rh(acac)_3$ in the nucleation and crystal growth stages has been shown to depend upon several synthetic parameters including an Ar or air atmosphere, reaction temperature and time, and $Rh(acac)_3$ concentration. Due to the present well-controlled polyol reduction kinetics, the size of the Rh nanocrystals can be tuned by changing the $Rh(acac)_3$ concentration in a proper range. Monolayer films of the Rh polygons have been formed on silicon wafers by the Langmuir−Blodgett method and have been used as model heterogeneous catalysts for the study of ethylene hydrogenation.

Introduction

Noble metal nanocrystals with controlled size, shape, chemical composition, and surface structure are of fundamental and technological importance because of their unique catalytic activity and selectivity and are employed for applications such as fine chemicals synthesis, oil refining processes, and fuel cell technology.[1−3] The ability to control shape, size, and size dispersity makes such nanocrystals ideal building blocks for constructing two- and three-dimensional (2-D and 3-D) model heterogeneous catalysts on various supports (e.g., silicon wafers, mesoporous oxide materials including SiO_2, Al_2O_3, and Ta_2O_5).[1f−h,2] Monodisperse noble metal nanocrystals have size- and shape-defined fractions of surface atoms and catalytically relevant structural attributes such as exposed crystal faces and the ratio of corner, edge, and terrace atoms. These properties make monodisperse nanocrystals good candidates for model catalytic studies and new catalytic technologies. Comprehensive understanding of the size/shape-dependent catalytic properties of noble metal nanocrystals (with respect to their bulk counterparts) and metal−support interactions can help to advance the development of heterogeneous catalysis theories and impact the fabrication of high-performance noble metal nanocatalysts for practical applications. Certainly, the elucidation of size/shape−function relationships requires the exploration of new synthetic methods that can provide improved size/shape control in a reproducible manner.

Recently, much attention has been paid to the size/shape control of noble metal nanocrystals (Rh,[4] Ir,[5] Pd,[6] Pt,[1a,g,2a,7] Ag,[8] Au[9]) by tuning the crystal growth kinetics in some solution-phase syntheses, including seeded growth by polyol reduction,[4a,b] modified polyol methods,[1a,f,g,4c,6,7a,8a,9a] thermolysis of organometallics,[4d,5] and micelle techniques.[7b,8b,9b] Because Rh is one of the most important noble metals, Rh nanocatalysts are used in a wide range of heterogeneous reactions such as hydrogenation, hydroformylation, and hydrocarbonylation.[4d,10] The size and shape control of Rh nanocrystals has thus become an important research focus. For example, the Somorjai and Tilley groups[4a,b] have reported the size and shape control of Rh nanocrystals (multipods, cubes, horns and cuboctahedra) by seeded growth in a polyol system. Xia and co-workers[4c] investigated the polyol synthesis and stability of Rh multipods, which show interesting surface plasmonic properties. By a nonhydrolytic organometallic approach, Son and co-workers[4d] prepared monodisperse oleylamine-capped Rh tetrahedral nanocrystals, which display excellent hydrogenation activity with a range of arenes. However, there has been little work on the size control of monodisperse Rh nanocrystals over a wide range, or the synthesis of multiple (111) twinned Rh particles, prior to this study.

In this paper, we report a one-step polyol synthesis of monodisperse, well-shaped Rh nanocrystals in the size range 5−15 nm at temperatures of 170−230 °C using rhodium(III) acetylacetonate [$Rh(acac)_3$] as the source of metal ions, 1,4-butanediol as the reducing solvent, and poly(vinylpyrrolidone) (PVP) as the capping agent. The nanocrystals are composed of

* Corresponding author: e-mail somorjai@berkeley.edu.
† University of California and Lawrence Berkeley National Laboratory.
‡ Peking University.

10.1021/jp073350h CCC: $37.00
Published on Web 08/02/2007

hexagons, pentagons, and triangles with (111) surfaces, which are recognized as catalytically active in face-centered-cubic metal particles.[1b,4d,11] The hexagons and pentagons have been identified as multiple (111) twinned particles. The mechanism of the polyol synthesis of the Rh nanocrystals is discussed by considering the $Rh(acac)_3$ reduction kinetics in the nucleation and crystal growth stages. Additionally, a Langmuir−Blodgett (LB) trough was used to fabricate monolayer films of the size-tunable Rh nanocrystals on Si wafers as model 2-D catalysts. Catalytic results of ethylene hydrogenation over the PVP-capped Rh nanocrystal LB films confirm that the samples are active catalysts for hydrogenation reactions.

Experimental Section

1. Chemicals. Rhodium(III) acetylacetonate [$Rh(acac)_3$, 97%], 1,4-butanediol (99%; bp 230 °C), poly(vinylpyrrolidone) (PVP, $M_w = 55\,000$), and acetylacetone (Hacac, ≥99%) were purchased from Sigma−Aldrich. All solvents, including acetone, ethanol, hexane, and chloroform, were of analytical grade and were used without further purification.

2. Synthesis of Rh Nanocrystals. Given amounts of $Rh(acac)_3$ [1.25−200 mg, $(0.0313-5) \times 10^{-4}$ mol] and PVP [3.47−555 mg, $(0.0313-5) \times 10^{-3}$ mol in terms of the repeating unit] at a fixed Rh/PVP ratio of 1:10 were added to 20 mL of 1,4-butanediol in a 50 mL three-necked flask at room temperature. The stock solution was heated to 140 °C in a Glas-Col electromantle (60 W; 50 mL) with a Cole-Parmer temperature controller (Diqi-sense), and was evacuated at this temperature for 20 min to remove water and oxygen under magnetic stirring, resulting in an optically transparent orange-yellow solution. The flask was then heated to the desired reaction temperature, between 170 and 230 °C, at a rate of 10 °C min^{-1}, and maintained at this temperature (±2 °C) for 2 h under Ar. During the reaction, the color of the solution gradually turned from orange-yellow to black. When the reaction was complete, an excess of acetone was poured into the solution at room temperature to form a cloudy black suspension. This suspension was separated by centrifugation at 4200 rpm for 6 min, and the black product was collected by discarding the colorless supernatant. The precipitated Rh nanocrystals were washed with acetone once and then redispersed in ethanol.

3. Fabrication of Langmuir−Blodgett Films. The Rh nanocrystals were washed several times by precipitation/dissolution in ethanol and then in chloroform (1 mL of Rh dispersion was precipitated by adding 4 mL of hexane and redispersed in 1 mL of ethanol or chloroform with sonication), to remove the impurities and excess PVP. Monolayers of Rh nanocrystals were formed by placing drops of Rh nanocrystal chloroform solution onto the water subphase of a LB trough (Nima Technology, M611) at room temperature.[2a] The surface pressure was monitored with a Wilhelmy plate and was adjusted to zero before the nanocrystals were spread. The resulting surface layer was compressed by moving the mobile barrier such that the film surface area decreased at a rate of 15 cm^2/min. At different stages of compression, the Rh layers at the water−air interface were carefully transferred onto continuous carbon-coated copper grids by the Langmuir−Schäffer horizontal liftoff method. The surface coverage was evaluated by counting the particles on the same area of the copper grid. The Rh nanocrystals were deposited onto Si wafers (1 cm × 1 cm) by lift-up of the substrates at a rate of 1 mm/min.

4. Characterization Methods. The shape, size, and lattice structure of the Rh nanocrystals were analyzed on a Philips FEI Tecnai 12 transmission electron microscope (TEM) and Philips CM200/FEG high-resolution (HR) TEM, operated at 100 and 200 kV, respectively. The samples were prepared by placing a drop of a Rh nanocrystal sol in ethanol onto a continuous carbon-coated copper TEM grid. Powder X-ray diffraction (XRD) patterns were recorded on a Bruker D8 GADDS diffractometer using Co Kα radiation ($\lambda = 1.79$ Å). All UV−vis absorption spectra were measured on an Agilent 8453 UV−visible ChemStation equipped with a 1 cm path length quartz cuvette, with the samples prepared by diluting 0.1 mL of reaction solution (aspirated directly from the reaction system with a 1 mL plastic syringe) with 5 mL of absolute ethanol. X-ray photoelectron spectrometric (XPS) experiments were performed on a Perkin-Elmer PHI 5300 XPS spectrometer with a position-sensitive detector and a hemispherical energy analyzer in an ion-pumped chamber (evacuated to 2×10^{-9} Torr). The Al Kα ($BE = 1486.6$ eV) X-ray source of the XPS spectrometer was operated at 300 W with 15 kV acceleration voltage. The binding energy (*BE*) for the samples was calibrated by setting the measured *BE* of C 1s to 285 eV. The elemental ratio was calculated from the integrated peak areas of the Rh 3d and O 1s core levels, showing a deviation of around 10%. Fourier transform infrared (FTIR)−diffuse reflectance infrared Fourier transform (DRIFTS) spectra were measured with a Nicolet Nexus-670 spectrophotometer with integrated diffuse reflectance optics (Spectra-Tech Collector II).

5. Ethylene Hydrogenation. Catalytic reactions were studied in a Pyrex reactor connected to a $^1/_4$-in. stainless steel manifold containing mass flow controllers (Unit Instruments) for delivery of reactant gases. Ethylene (AirGas, CP grade), hydrogen (Praxair, UHP, 99.999%), and helium (Praxair, UHP, 99.999%) were used as received. The catalyst was mounted on a stainless steel cell with an O-ring seal and a kapton heater mounted to the back of the sample (22.5 mm^2 in area). The temperature was measured by a thermocouple in contact with the front of the sample. Reactants and products were detected by gas chromatography (Hewlett-Packard 5890) and quantified by use of Dietz tables.[12] Reaction rate measurements were conducted at differential conditions (all conversions, $X < 10\%$). Prior to each catalytic test, the sample was pretreated first by heating to 90 °C in vacuum and then by reducing in 200 Torr H_2 with He as a makeup gas at 90 °C. All measurements were taken at 200 Torr H_2 and 20 Torr ethylene. The turnover frequency (TOF) was calculated from the surface coverage and sample size by assuming that the Rh nanocrystals were spherical and nonoverlapping.

Results and Discussion

1. Size, Shape, and Surface Structure. By use of the polyol method, monodisperse Rh nanocrystals in the size range of 5−15 nm were prepared (Table 1 and Figure 1 see also Figures S1 and S2 in Supporting Information). TEM measurements show that the Rh nanocrystals have various polygonal shapes in 2-D projections, including hexagons, pentagons, triangles, squares, and rhombohedra, among which the former three dominate. As seen from Figure 1a, 6.5 nm Rh nanocrystals are mainly composed of hexagons with a yield of 74%. The HRTEM analyses reveal that the nanocrystals have (111) surface structures (interplanar distance 0.21 nm), with observable {111} twins (Figure 1b). In addition, the nanocrystals exhibit significant lattice distortions, indicating that they are highly strained, possibly due to the existence of a high density of defects on their surfaces.[13] Figure 1c shows that the 13.5 nm Rh nanocrystals are composed of 36% hexagons, 26% pentagons, and 17% triangles (see Table 1). The hexagons and pentagons appear

TABLE 1: Shape, Size, and $I_{(111)}/I_{(200)}$ Ratio of Monodisperse Rh Nanocrystals Synthesized in 1,4-Butanediol under Ar

					shape (yield, %)					
entry	$Rh(acac)_3$ (mM)	PVP (mM)	T (°C)	t (h)	hexagon	pentagon	triangle	no. counted	size (nm)	$I_{(111)}/I_{(200)}$
1	0.313	3.13	225	2	>95			150	5.4 ± 0.5[a]	10.8
2	0.625	6.25	225	2	74		15	141	6.5 ± 0.5	12.5
3	1.25	12.5	225	2	39	16	14	278	7.1 ± 0.5	11.0
4	1.25	12.5	195	2	38	20	14	126	7.7 ± 0.7	4.71
5	1.25	12.5	205	2	33	22	22	162	8.3 ± 0.7	4.78
6	2.5	25	225	2	33	15	18	251	9.3 ± 0.8	3.69
7	5	50	225	2	36	22	12	174	10.7 ± 0.9	3.62
8	5	50	205	2	36	26	17	178	13.5 ± 1.4	4.22

[a] Standard deviation statistic from 150 nanocrystals.

to have {111} twin planes (Figure 1d,e), while the perfect triangles (thermodynamically equilibrium shape) and imperfect triangles (thermodynamically nonequilibrium shape)[13a] are both single-crystalline with exposed (111) facets (Figure 1f,g). The presence of a 5-fold symmetry axis in the HRTEM images of the pentagons indicates that they are multiple twinned particles (MTPs) such as decahedra. Moreover, the clear lattice fringes observed from the HRTEM images (Figure 1b,d−g) confirm that as-synthesized Rh nanocrystals are highly crystalline, showing no appreciable amorphous phases.

The yields of hexagons, pentagons, and triangles are listed in Table 1. The 5.4 nm Rh nanocrystals are made up of >95% hexagons (Figure 1h), while the 7.7 nm nanocrystals contain 38% hexagons, 20% pentagons, and 14% triangles (Figure 1i). The 8.3 nm nanocrystals contain 33% hexagons, 22% pentagons, and 22% triangles (Figure 1j), while 9.3 nm nanocrystals are composed of 33% hexagons, 15% pentagons, and 18% triangles (Figure 1k). The total yield of the hexagons, pentagons, and triangles for the Rh nanocrystals is greater than 65% for each sample.

Line broadening observed in the X-ray diffractograms indicates that all of the samples are nanocrystalline in nature (Figure 2). Three well-resolved diffraction peaks at 49.2°, 57.4°, and 85.0° in 2θ value are ascribed to the (111), (200), and (220) crystal planes of face-centered-cubic (fcc) Rh metal (JCPDS 5-685). As listed in Table 1, the ratios of $I_{(111)}/I_{(200)}$ for the Rh polygons described here are in the range of 3.62−12.5, which are significantly higher than 1.82 for 12.7 nm Rh cubes [enclosed by six (100) facets],[4a] and 3.1 for 4.87 nm Rh cuboctahedra [enclosed by six (100) facets and eight (111) facets].[4b] This result strongly suggests that the Rh nanocrystals are dominated by (111) surface structures, which is consistent with the HRTEM results.

2. Formation Conditions of Rh Nanocrystals. Alcohol reduction has been developed as a general approach for the synthesis of colloidal metal nanoparticles since the 1990s.[1a,b,d,e,2,4a−c,6,7a,8a,9a] The size/shape control by this method is known to be governed by several factors, such as the reduction kinetics of a metal precursor by an alcohol (related to the intrinsic physical and chemical behaviors of a noble metal and its precursor compound and the reducing power of an alcohol), the crystal growth regime (kinetic or thermodynamic), the coordinating ability of a capping agent, and the chemical environment inside the reaction medium (oxidative or inert). In this work, a set of condition-dependent experiments was carefully carried out to reveal the effects of various synthetic parameters on the Rh nanocrystal characteristics (such as size distribution and shape). An Ar or air atmosphere, reaction temperature and time, and $Rh(acac)_3$ concentration have been demonstrated to be crucial factors responsible for the formation of monodisperse Rh nanocrystals with well-defined shapes.

Effect of an Argon or Air Atmosphere. An oxidative atmosphere during the polyol synthesis leads to partial oxidization of Rh(0) atoms into Rh(III/IV) oxides, especially at high reaction temperatures (>195 °C). Figure 3 displays the XPS survey spectra of Rh nanocrystals synthesized under different ambient conditions at 225 °C with $[Rh(acac)_3] = 1.25$ mM. The identified peaks are assigned to the core levels of Rh 3p ($3p_{1/2}$, 521 eV; $3p_{3/2}$, 496 eV), Rh 3d ($3d_{3/2}$, 310 eV; $3d_{5/2}$, 306 eV), O 1s (531 eV), N 1s (399 eV), and C 1s (285 eV). The appearance of the intense peaks of C 1s and O 1s, together with the weak peak of N 1s, is mainly due to the PVP capping agent on the surface of Rh nanocrystals (also see the FTIR results; Figure S3 in Supporting Information). Recently, it was reported that Rh species with different valences could be differentiated by the position of the Rh $3d_{5/2}$ peak. For Rh(0), Rh_2O_3, and RhO_2 thin films, the binding energies (*BE*) of Rh $3d_{5/2}$ are 307.2, 308.3, and 308.6 eV, respectively.[14] Considering such *BE* differences, further fitting of the Rh 3d and O1s peaks of our XPS spectra discloses that the atomic ratio of Rh(III/IV) to Rh(0) is 0.17 for the nanocrystals synthesized under Ar, which is lower than that (0.23) for the nanocrystals synthesized under air (Figure 4). In addition, the atomic ratio of O to Rh is 8.5 for the nanocrystals synthesized under Ar, which is nearly half that (18) for the nanocrystals synthesized under air. As a result, we conclude that Rh nanocrystals synthesized under air contain a larger proportion of oxide species, which are generated from the much stronger continuous oxidative etching on the nanocrystal surfaces by abundant oxygen in open air during the synthesis.

Further characterization reveals that an oxidative atmosphere during nanocrystal growth also has an impact on the size distribution and morphology of Rh nanocrystals. Figure 5 shows TEM images of Rh nanocrystals synthesized at 225 °C for 2 h under Ar and air ($[Rh(acac)_3] = 5$ mM). The Rh nanocrystals synthesized under Ar consist of 36% hexagons, 22% pentagons and 12% triangles (estimated from 174 nanocrystals) with an average diameter of 10.7 nm (SD 8.4%) (Figures 5a, S1g, and S2g). However, the nanocrystals synthesized under air are composed of 30% hexagons, 30% pentagons and 19% triangles (estimated from 105 nanocrystals), and display enlarged size and size distribution (12.3 nm, SD 15%, Figure 5b;see also Figure S4 in Supporting Information). The total yield of MTPs (hexagons and pentagons) is equal for the two samples, indicating that oxidative condition during Rh nanocrystal growth does not remove the twinned particles, unlike the case of the polyol synthesis of uniform Pd nanocrystals.[6b] Additionally, the Rh polygons synthesized under inert Ar gas show straighter edges and sharper corners than those obtained under air (insets in Figure 5a,b). In summary, synthesis of Rh nanocrystals under an inert Ar atmosphere resulted in more monodisperse and well-shaped particles than synthesis under air. For this reason, all other syntheses in this study have been performed under Ar.

Effect of Reaction Time. Through TEM measurements, we investigated the crystal growth of Rh nanocrystals with time at

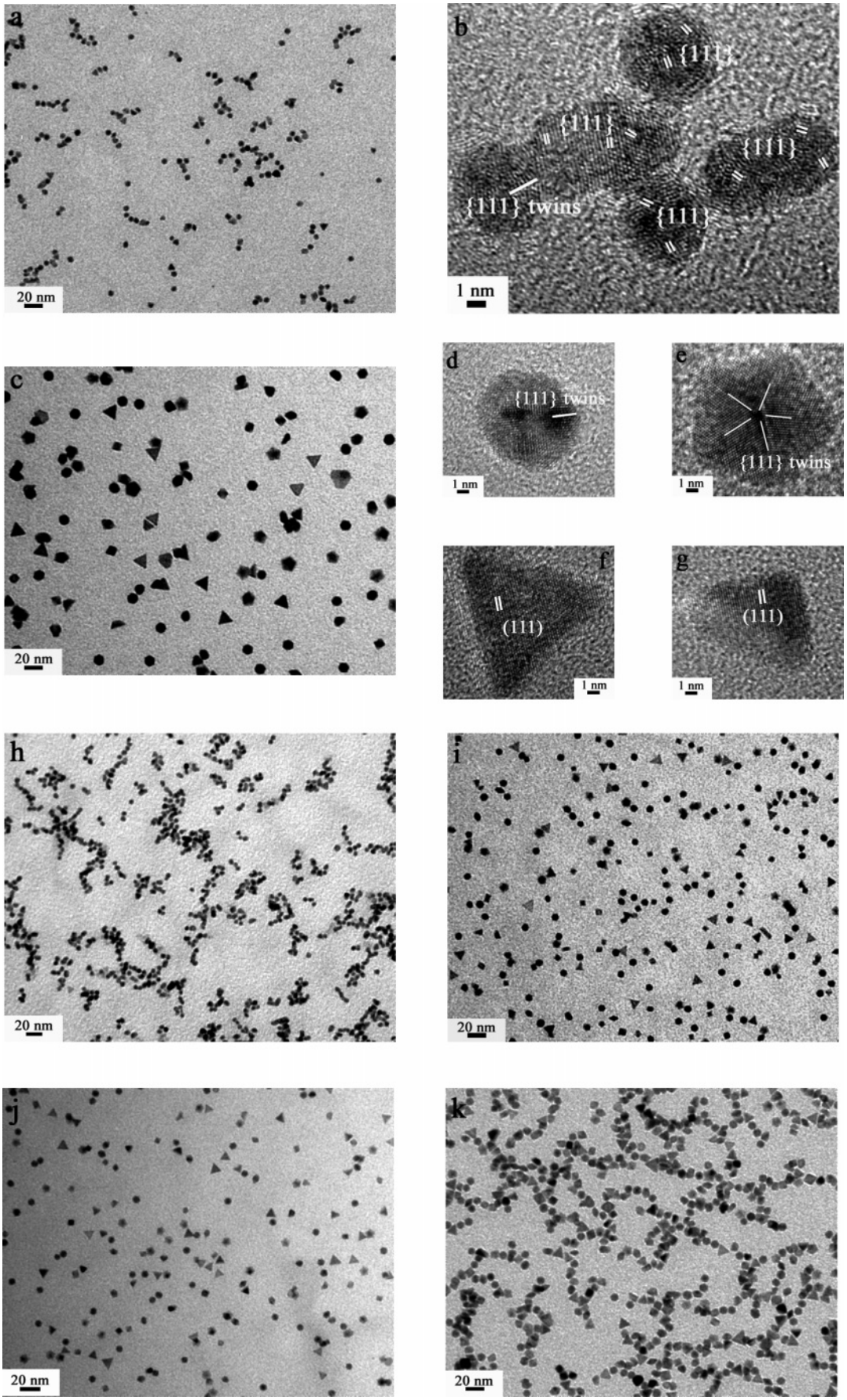

Figure 1. (a) TEM and (b) HRTEM images of 6.5 nm Rh nanocrystals. (c) TEM and (d−g) HRTEM images of 13.5 nm Rh nanocrystals. (h−k) TEM images of (h) 5.4, (i) 7.7, (j) 8.3, and (k) 9.3 nm Rh nanocrystals.

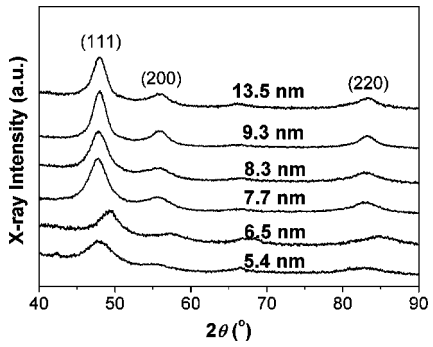

Figure 2. XRD patterns of as-synthesized Rh nanocrystals.

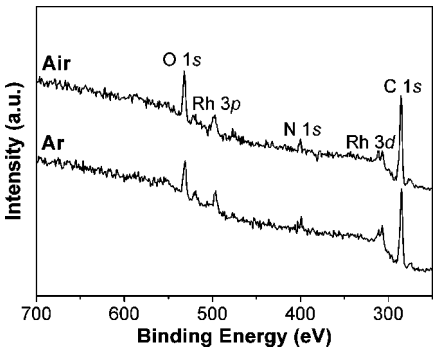

Figure 3. XPS survey spectra of Rh nanocrystals synthesized under Ar and air at 225 °C for 2 h ([$Rh(acac)_3$] = 1.25 mM).

215 °C under Ar ([$Rh(acac)_3$] = 12.5 mM). As the temperature was increased from 140 to 195 °C in 5 min, the color of the solution gradually turned from orange-yellow to dark brown, indicating the formation of Rh nanocrystals as the $Rh(acac)_3$ was reduced by 1,4-butanediol. The Rh product consisted of small particles (~4 nm) and large polygons (~15 nm), indicating instant nucleation and subsequent rapid crystal growth (68% of nanocrystals smaller than 10 nm; Figure 6a). As the temperature subsequently rose to 215 °C in another 5 min, 11 nm Rh nanocrystals (34% of nanocrystals smaller than 10 nm) with undefined shapes were formed (Figure 6b). After 15 min of reaction at 215 °C, the Rh nanocrystals rapidly grew to 15.9 nm (7.3% of nanocrystals smaller than 10 nm) as the smaller crystals were consumed. Meanwhile, the crystalline shapes developed highly faceted edges (Figure 6c). By 30 min, the nanocrystals were 16.1 nm in size (4.7% of nanocrystals smaller than 10 nm). At 45 min, the Rh nanocrystals enlarged to 16.6 nm at the complete expense of the small ones (2.1% of nanocrystals smaller than 10 nm; Figure 6d). At longer reaction times of 90, 120, and 180 min, the Rh nanocrystals showed no obvious changes in size, size distribution, or shape. Therefore, it is assumed that Ostwald ripening took place in 45 min during the growth of Rh nanocrystals.[9a]

Effect of Reaction Temperature. $Rh(acac)_3$ can be reduced to Rh(0) by 1,4-butanediol at temperatures above 170 °C under Ar. Panels a−c of Figure 7 show TEM images of Rh nanocrystals synthesized at different temperatures for 2 h under Ar ([$Rh(acac)_3$] = 5 mM). Below 195 °C, the Rh nanocrystals are polydisperse and not well-shaped (Figure 7a,b). The nanocrystals formed at this temperature were mainly twinned particles, favored by thermodynamics,[6b] but many were nanorods, favored by kinetics.[15] At a reaction temperature of 195 °C, 11.9 nm Rh nanocrystals were formed (SD 18%; Figure 7c). For reactions carried out at 205 and 225 °C, monodisperse Rh nanocrystals of 13.5 nm (SD 10%; Figure 1c) and 10.7 nm (SD 8.4%; Figure 5a), respectively, were formed. It should be noted that the size distribution of the Rh nanocrystals synthesized at 225 °C was significantly narrowed, although the size decreased considerably for [$Rh(acac)_3$] = 5 or 1.25 mM (Figure 7d), indicating that a balance between the reduction rate of $Rh(acac)_3$ and crystal growth stages is reached at this temperature, resulting in nanocrystals of uniform size. Furthermore, we see that the size of the Rh nanocrystals synthesized with [$Rh(acac)_3$] = 1.25 mM are considerably smaller and have a narrower size distribution than those synthesized with [$Rh(acac)_3$] = 5 mM at temperatures of 195−225 °C because a low $Rh(acac)_3$ concentration favors a decreased growth rate of the nanocrystals.

Effect of $Rh(acac)_3$ Concentration. At a given reaction temperature, the size of the Rh nanocrystals can be tuned by changing the concentration of $Rh(acac)_3$. For example, at 225 °C with [$Rh(acac)_3$] = 0.156 mM, the resulting Rh nanocrystals are 6.4 nm in size (SD 17%; Figure 8a). With a doubling in precursor concentration ([$Rh(acac)_3$] = 0.313 mM), the Rh nanocrystals become more monodisperse with a size of 5.4 nm (SD 9.0%; Figures 8a 1h, S1a, and S2a). Between 0.313 and 5 mM $Rh(acac)_3$, the resulting nanocrystal size increases with increasing concentration while the percent standard deviation in size remains constant at ~8%. Particles with a mean diameter of 6.5 nm (SD 7.7%; Figures 8a 1a, S1b, and S2b), 7.1 nm (SD 7.0%; Figures 8a, S1c, and S2c), 9.3 nm (SD 8.6%; Figures 8a, 1k, S1f, and S2f), and 10.7 nm (SD 8.4%; Figures 8a, 5a, S1g, and S2g) were synthesized with [$Rh(acac)_3$] = 0.625, 1.25, 2.5, and 5 mM, respectively. Increasing the concentration to 10 mM formed larger 13.5 nm particles with a broadened size distribution (SD 16%; Figure 8a). At a concentration of 25 mM, the nanocrystals again become smaller in size (9.5 nm) but still have a large size distribution (SD 19%; Figure 8).

3. Formation Mechanism of Rh Nanocrystals. In order to obtain improved size/shape control for colloidal noble metal nanoparticles, intensive research has been devoted to the manipulation of reduction kinetics of the metal precursors in the nucleation and crystal growth stages involved in polyol methods.[2a,4a−c,6,7a,8a,9a,15] It is believed that control of the reduction kinetics is a key to the formation of monodisperse nanocrystals with well-defined shape. The formation of monodisperse Rh nanocrystals by the polyol method described here is simply illustrated in Scheme 1.

We observe that $Rh(acac)_3$ dissolves completely in 1,4-butanediol upon heating above 110 °C, forming a transparent orange-yellow solution. As the solution is heated to 175 °C under Ar, the reduction of $Rh(acac)_3$ by 1,4-butanediol starts, characterized by the appearance of a color change. By either extending the reaction time at 175 °C or raising the reaction temperature above 175 °C, we observe a sequential color change from orange-yellow, to red, to brown, to dark brown, and finally to black. This chemical phenomenon indicates the gradational reduction of $Rh(acac)_3$ by 1,4-butanediol, presumably because the strongly chelating Rh−O bonds in the $Rh(acac)_3$ complex slow reduction. Therefore, Rh(0) atoms can be gradually produced from the controlled reduction of $Rh(acac)_3$.

Analysis of UV−vis spectroscopic measurements shows that PVP and Hacac ligands display very strong absorption peaks at 208 and 273 nm, respectively, while $Rh(acac)_3$ has peaks at 318 (moderately strong), 258 (weak), and 204 nm (very strong) (see Figure S5 in Supporting Information). The peak at ~320 nm is characteristic of $Rh(acac)_3$ and can be used to monitor the consumption of $Rh(acac)_3$ with time and temperature. Figure 9 shows UV−vis spectra for reaction aliquots under various conditions and after different reaction times. In contrast to the UV−vis spectrum of pure $Rh(acac)_3$ (Figure S5), those taken

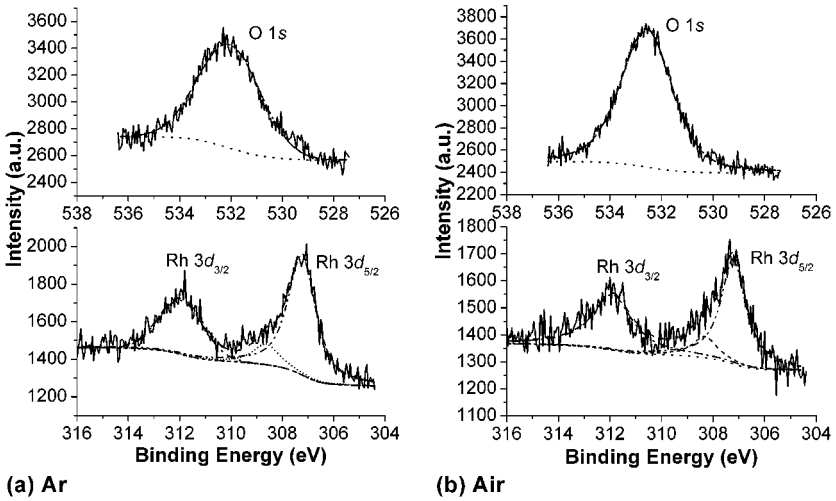

Figure 4. Rh 3d and O 1s XPS signals recorded for Rh nanocrystals synthesized under (a) Ar and (b) air at 225 °C for 2 h ([$Rh(acac)_3$] = 1.25 mM).

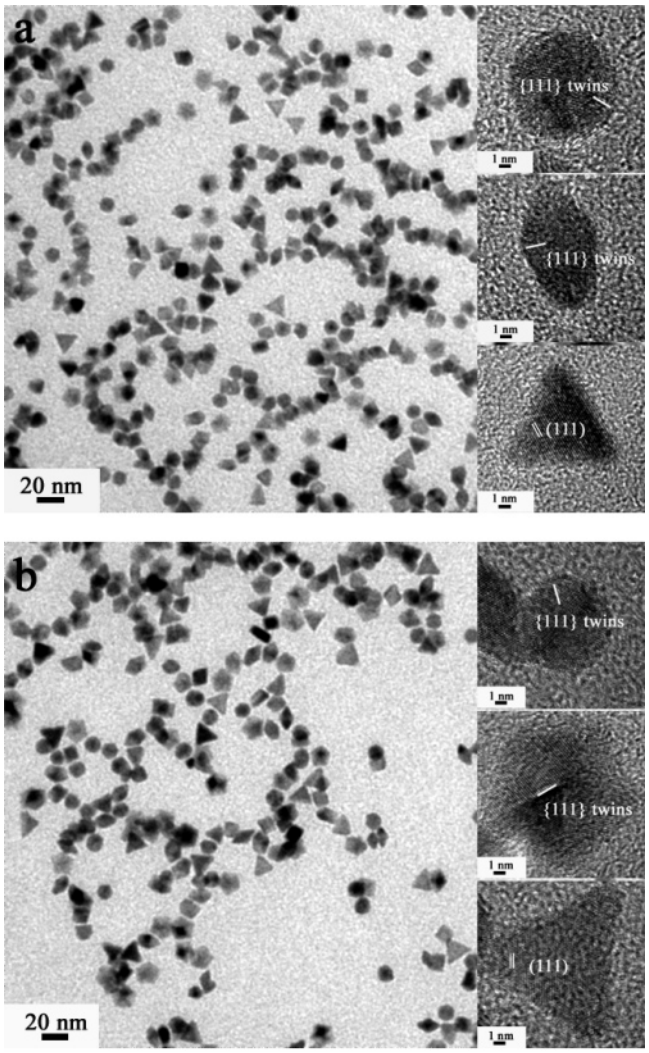

Figure 5. TEM and HRTEM (inset) images of Rh nanocrystals synthesized at 225 °C for 2 h under (a) Ar and (b) air ([$Rh(acac)_3$] = 5 mM).

during reduction show increased intensity for the peak at 265 nm relative to that at 320 nm, probably indicative of the formation of Hacac species following reduction of $Rh(acac)_3$ by 1,4-butanediol. From Figure 9a, we can see that $Rh(acac)_3$ is not completely reduced at 175 or 185 °C after 2 h for [$Rh(acac)_3$] = 5 mM, as suggested by the presence of the peak at 320 nm. At 195 °C, this peak disappears, corresponding to the complete reduction of $Rh(acac)_3$ after 2 h (Figure 9a). It was found that $Rh(acac)_3$ can be completely reduced in 30 min at 215 °C and 12.5 mM $Rh(acac)_3$ (see Figure 9b). The depletion of the peak at ~320 nm for $Rh(acac)_3$ with time observed in the UV−vis spectra (Figure 9b) and the size evolution observed in the TEM micrographs (Figure 6) indicate that the consumption of $Rh(acac)_3$ occurs during nucleation and also in the early stages of nanocrystal growth. Additionally, higher temperatures favor faster reduction and more rapid $Rh(acac)_3$ consumption (Figure 9a).

For a fixed reaction temperature, it is noted that higher $Rh(acac)_3$ concentrations leads to faster reduction. For instance, when heating reaction solutions with [$Rh(acac)_3$] = 12.5 and 5 mM, the orange-yellow to black color change occurs at 195 and 210 °C, respectively, with identical heating rates. With [$Rh(acac)_3$] = 1.25 mM, this color change occurs at 225 °C. An appropriate reduction rate for the growth of monodisperse Rh nanocrystals is obtained at temperatures in excess of 190 °C and with low $Rh(acac)_3$ concentrations in the range 0.313−5 mM. At a given temperature, a lower $Rh(acac)_3$ concentration gives a slower reduction rate and decreased consumption of Rh atoms during crystal growth, resulting in a slower growth rate of Rh nanocrystals. Under this condition, smaller monodisperse Rh nanocrystals are produced. Consequently, the size of Rh nanocrystals decreases with the $Rh(acac)_3$ concentration within the range 0.313−5 mM. This case is similar to the growth of monodisperse Rh nanoparticles by the seeded growth method, that is, the addition of fewer monomers yields smaller nanocrystals.[4a,b] However, when the $Rh(acac)_3$ concentration is lower than 0.313 mM, a decreased reduction rate continuously produces Rh(0) atoms over a long period of time while suppressing Ostwald ripening. In this case, polydisperse Rh nanocrystals are formed (see Figure 8a). On the other hand, at concentrations greater than 5 mM, the rapid reduction rate generates many Rh(0) atoms in a short period of time for consumption during the crystal growth stage while suppressing Ostwald ripening, resulting in size polydispersity (see Figures 8a and 6).

It is well-known that the surface energies of fcc metals follow the order of (111) < (100) < (110) with the (111) surface being the most stable.[13] MTPs [(111) twinned structures] have the lowest free energy and are thus thermodynamically favored for

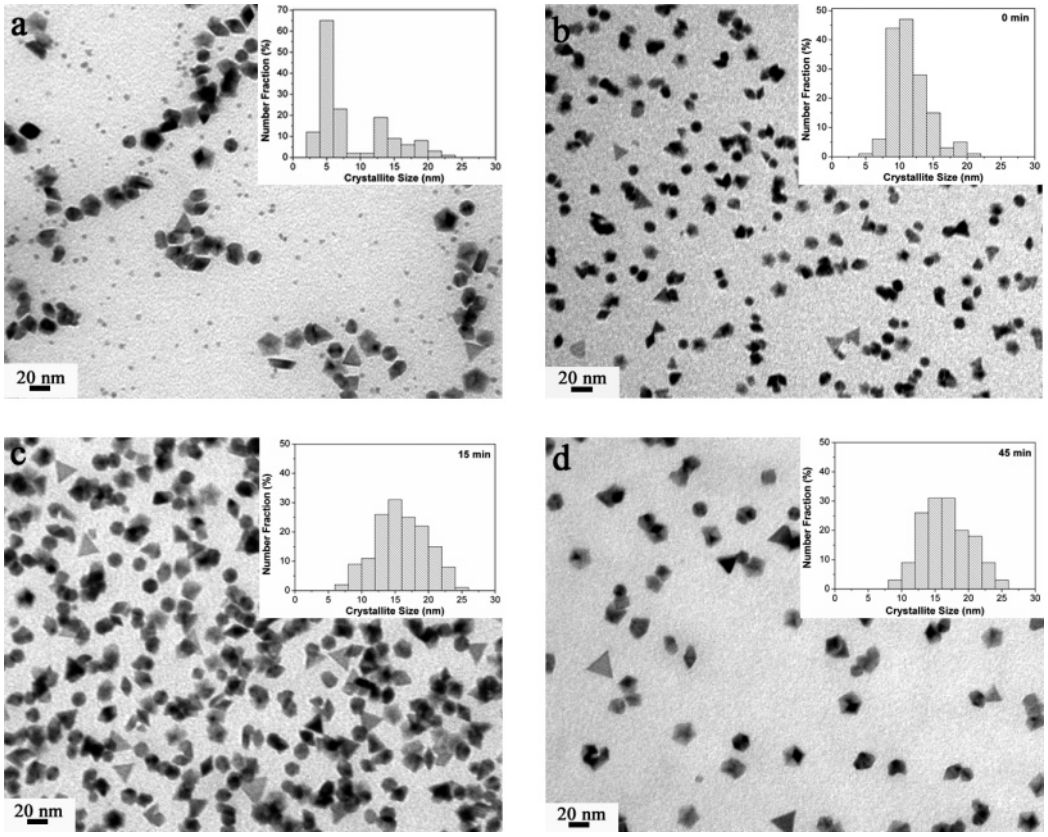

Figure 6. (a) TEM image of the Rh product collected at 195 °C as the temperature was elevated from 140 to 215 °C under Ar ([Rh(acac)$_3$] = 12.5 mM). (b−d) TEM images of Rh nanocrystals synthesized at 215 °C for different periods of time under Ar ([Rh(acac)$_3$] = 12.5 mM): (b) 0, (c) 15, and (d) 45 min. (Insets: size distribution histograms from 150 Rh nanocrystals.)

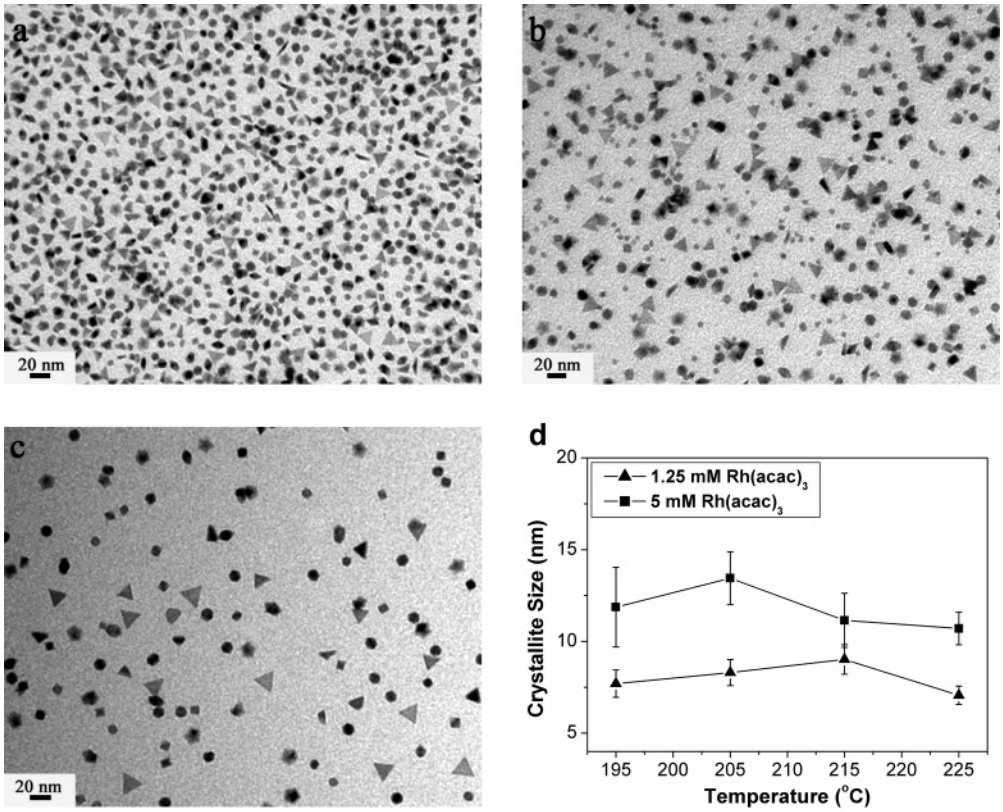

Figure 7. (a−c) TEM images of Rh nanocrystals synthesized at different temperatures for 2 h under Ar ([Rh(acac)$_3$] = 5 mM): (a) 175, (b) 185, and (c) 195 °C. (d) Plot of the size of the Rh nanocrystals as a function of temperature.

fcc noble metals.[6,13] Considering that our fcc Rh polygons (hexagons, pentagons, and triangles) with (111) orientations are formed under a moderate reduction rate and relatively high reaction temperatures, and their morphologies appear unchanged

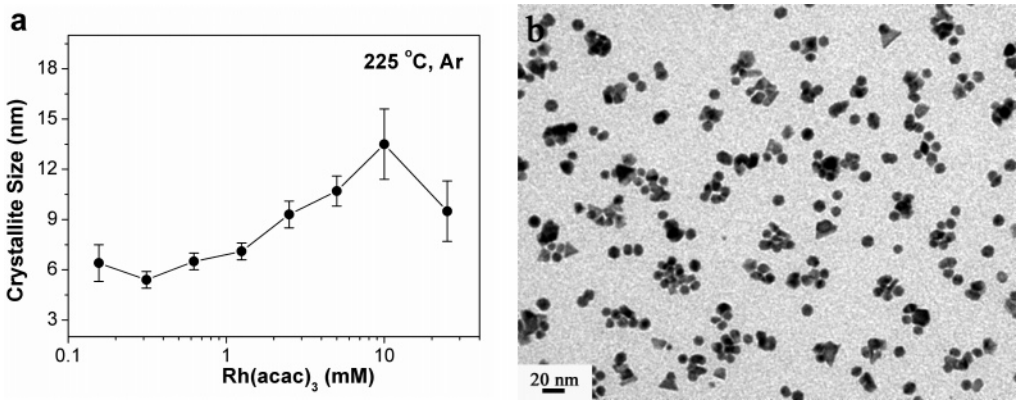

Figure 8. (a) Plot of the size of Rh nanocrystals synthesized at 225 °C for 2 h under Ar as a function of the $Rh(acac)_3$concentration. (b) TEM image of Rh nanocrystals synthesized at 225 °C for 2 h under Ar ($[Rh(acac)_3] = 25$ mM).

SCHEME 1: Schematic Illustration of One-Step Polyol Synthesis of Monodisperse Well-Shaped Rh Nanocrystals

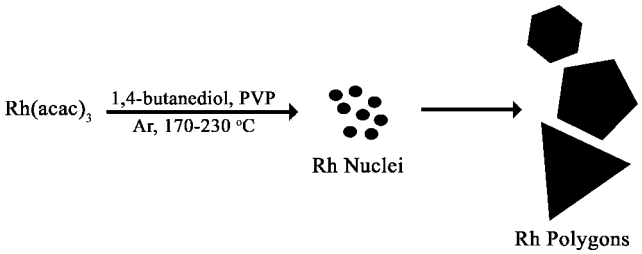

with time in the presence or absence of oxidative etching, these shapes can be considered thermodynamically stable.[6,13] Furthermore, the formation of Rh MTPs (hexagons and pentagons) in high population (>45%, see Table 1) is probably due to the high density of planar defects generated on the {111} planes of the Rh nanocrystals during synthesis.[6,13] From TEM measurements (see Figures 1c,i−k and 5a), the size of the polygons follows the trend hexagons < pentagons < triangles (as shown in Scheme 1); however, the reasons responsible for this are not yet understood.

4. Formation of LB Monolayers. The LB technique is a robust and versatile method for packing nanoscale building blocks[16] (such as quantum dots,[16b,c] nanorods,[16d] and nanowires[16e]) into long-range ordered 2-D arrays on different substrates. Recently, this method has been successfully employed to make dense LB monolayers of PVP-capped Pt nanocrystals with various shapes (cubes, cuboctahedra, and octahedra) for heterogeneous catalytic studies.[1f,2a,7b] In this work, we prepare monolayer films of size-tunable monodisperse Rh nanocrystals on Si wafers with a LB trough and investigate the effects of crystallite size on film formation.

After the Rh nanocrystals spread uniformly on the water surface in the LB trough, the resulting surface pressure is 2−4 mN/m, possibly due to the presence of PVP on the nanocrystal surfaces.[2a] Figure 10 shows TEM images of LB films formed at different surface pressures for 8.3 nm Rh nanocrystals. As the pressure steadily increases from 4.4 to 8.1 mN/m, and then to 10.4 mN/m due to compression by the mobile barrier, the surface coverage of Rh gradually increases from 11% (Figure 10a) to 24% (Figure 10b), and then to 33% (Figure 10c). At this stage, the Rh nanocrystals are discretely distributed on the substrates, showing no aggregation. As the pressure is further increased to 12.9 mN/m, the monolayer starts to collapse and forms multilayers, as revealed by the observation of nanocrystal aggregates on the TEM grid (surface coverage 53%; Figure 10d). As the LB film is further compressed, the surface pressure increases rapidly up to 23.3 mN/m, and Rh nanocrystal multilayers are formed (Figure 10e,f) with a surface coverage of 65−72%.

Figure 11a depicts the dependence of surface pressure on Rh nanocrystal surface coverage. The surface coverage for the 13.5 nm sample is lower than that of the 6.5 and 8.3 nm samples below 10 mN/m, perhaps as a result of the slightly larger size distribution of the former sample (Table 1). In this case, a broadened size distribution for the nanocrystals might prevent effective packing into monolayers at low surface pressures. Beyond 10 mN/m, the curves for the three samples are nearly coincident, indicating that monolayers can be made in the same surface pressure range. Experimentally, for our size-tunable Rh nanocrystals, monolayers form at surface pressures of 10−11 mN/m and have surface coverages of 35−64% (for example, see Figure 11b−d). These monolayer films demonstrate only very short-range order. It is assumed that the shape diversity observed for the Rh nanocrystals, together with the entangled long carbon chain and the hydrophilic pyrrolidone ring of PVP, limits long-range ordering.[2a]

5. Ethylene Hydrogenation. The LB films of Rh nanocrystals transferred onto Si wafers were tested for ethylene hydrogenation activity in a flow reactor. All samples were active for ethylene hydrogenation with turnover frequencies (TOF) of ~0.5 mol of ethane (mol of $Rh_s)^{-1}$ s^{-1}. The activity (in millimoles of ethane per square centimeter per minute) and TOF, along with the coverage of each LB sample, are listed in Table 2. The coverage was determined by measuring the fraction of the area of a TEM grid lifted off from the LB surface that was covered by Rh nanocrystals (see Figure 11). The number of surface Rh atoms on a sample was calculated by geometric considerations by approximating each particle as a sphere. Ethylene hydrogenation rates were measured between 313 and 373 K for each sample. At temperatures above 333 K, deactivation is rapid, likely due to the formation of a carbonaceous overlayer, making an accurate determination of apparent activation energy difficult. The absence of a particle size dependence on TOF is consistent with previous research showing that ethylene hydrogenation is structure-insensitive.[17] A TOF of ~0.5 mol of ethane (mol of $Rh_s)^{-1}$ s^{-1} is in the range of that reported for Rh clusters[18] and Rh single crystals.[19]

Conclusions

Using $Rh(acac)_3$ as the metal precursor, we have demonstrated the synthesis of monodisperse PVP-capped Rh polygons with tunable sizes ranging from 5 to 15 nm in 1,4-butanediol at temperatures of 170−230 °C under Ar. The polygons are

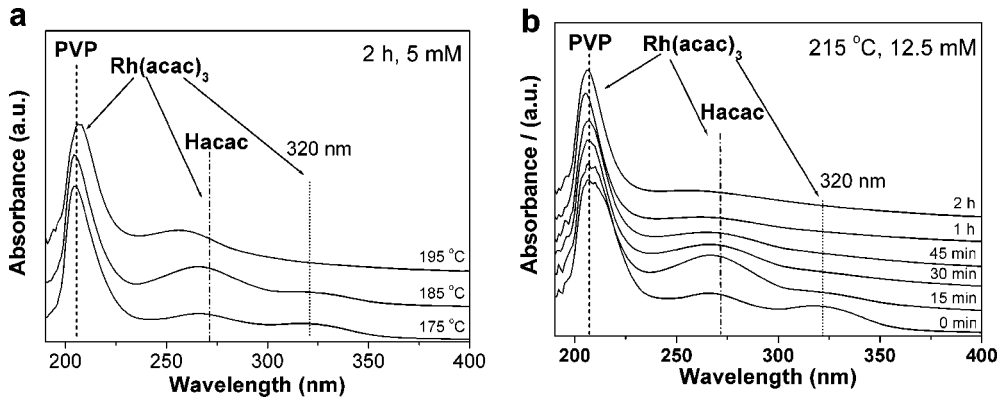

Figure 9. (a) UV−vis spectra of solutions taken at different temperatures after reacting for 2 h under Ar ($[Rh(acac)_3] = 5$ mM). (b) UV−vis spectra of solutions at increasing reaction times at 215 °C under Ar ($[Rh(acac)_3] = 12.5$ mM).

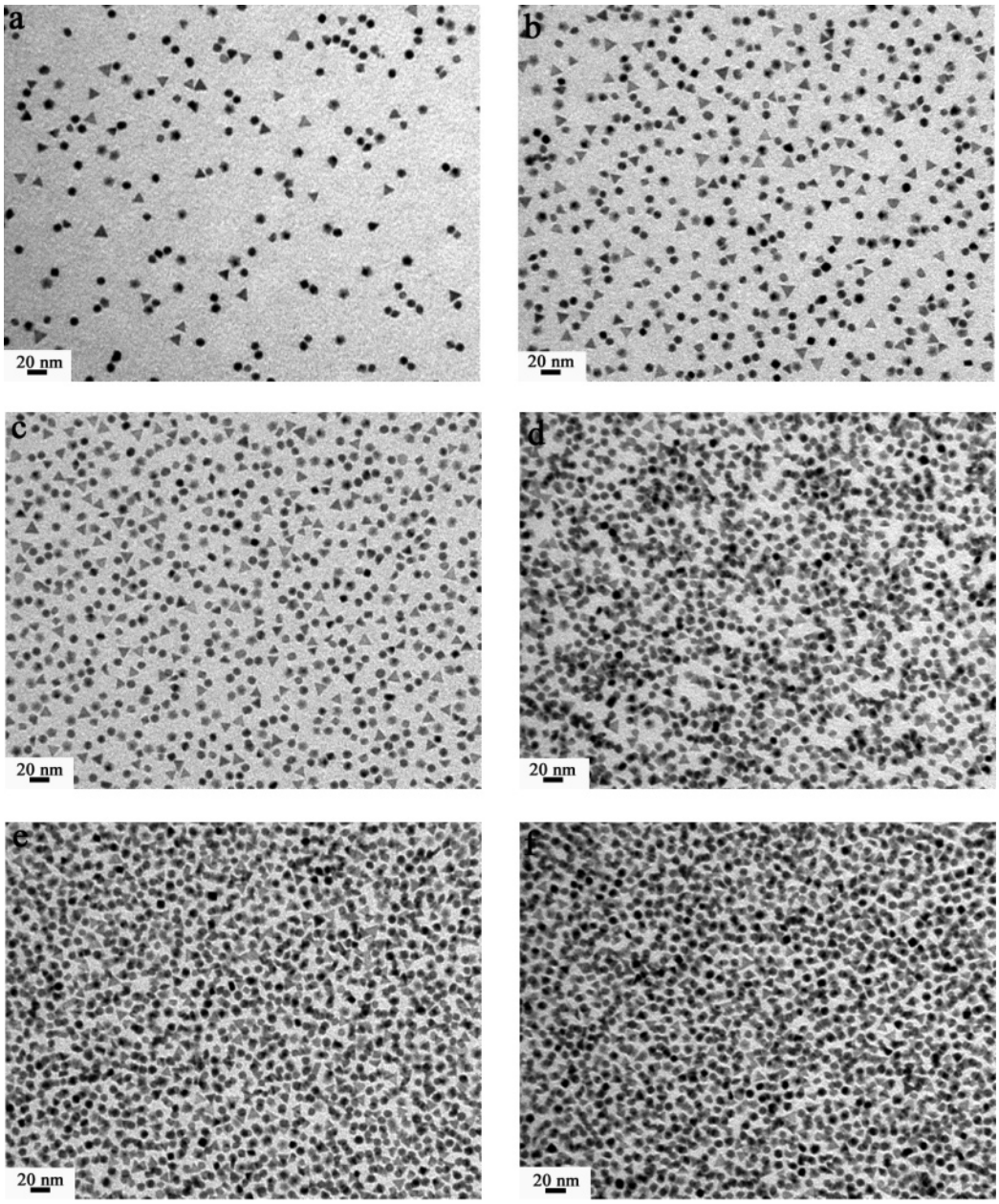

Figure 10. TEM images of Langmuir−Blodgett films of 8.3 nm Rh nanocrystals, formed under different surface pressures: (a) 4.4, (b) 8.1, (c) 10.4, (d) 12.9, (e) 16.6, and (f) 23.3 mN/m.

dominated by hexagons, pentagons, and triangles exposing (111) surfaces (>65% in yield). Due to the generation of planar defects of the {111} twins in the present synthesis, multiple (111) twinned particles including hexagons and pentagons were formed in a high yield (>45%). Without the use of seeds, the size of the Rh nanocrystals can be manipulated by varying the

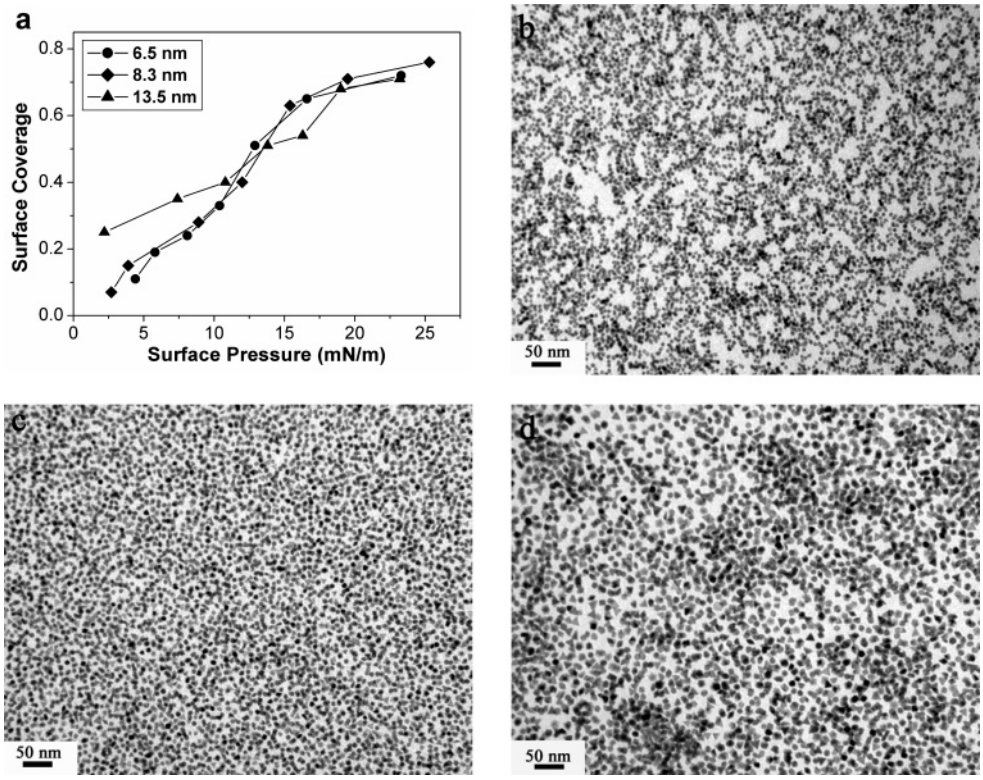

Figure 11. (a) Plot of the surface pressure as a function of the surface coverage of Rh Langmuir−Blodgett films. (b−d) TEM images of the LB monolayers of Rh nanocrystals: (b) 6.5 nm, 10.3 mN/m; (c) 8.3 nm, 10.8 mN/m; (d) 10.7 nm, 10.9 mN/m.

TABLE 2: Ethylene Hydrogenation Turnover Frequency for the LB Monolayers of Differently Sized Rh Nanocrystals on Silicon Wafers

size (nm)	coverage[a]	activity (mmol of ethane cm^{-2} min^{-1})	TOF[b] [mol of ethane (mol of Rh_s)$^{-1}$ s^{-1}]
6.5	0.53	0.20	0.59
7.1	0.32	0.10	0.51
7.7	0.56	0.14	0.40
8.3	0.56	0.16	0.44
9.3	0.53	0.19	0.57
10.7	0.64	0.21	0.52

[a] Coverage determined from a 1 μm × 1 μm area of a TEM grid lifted from LB trough. [b] Surface Rh (Rh_s) was determined from geometric considerations. Reaction conditions were 20 Torr ethylene, 200 Torr H_2, 550 Torr He, and 350 K.

$Rh(acac)_3$ concentration because of the well-controlled precursor reduction kinetics in the nucleation and crystal growth stages. The polyol method developed here has the merits of one-step synthesis, easy operation, and good reproducibility. Overall, it provides a good recipe for the size control of Rh nanocrystals in solution. By the LB technique, monolayer films were produced for the differently sized Rh nanocrystals on Si wafers, under nearly the same surface pressures. Preliminary catalytic tests reveal that the Rh nanocrystal monolayers are active for ethylene hydrogenation.

Acknowledgment. This work was supported by the Director, Office of Science, Office of Basic Energy Sciences, Division of Chemical Sciences, Geological and Biosciences of the U.S. Department of Energy under Contract DE-AC02-05CH11231. Y.Z. gratefully acknowledges the financial aid of the Huaxin Distinguished Scholar Award from Peking University Education Foundation of China. We thank the Berkeley Electron Microscopy Lab and National Center for Electron Microscopy for use of their TEM and HRTEM facilities, and we also thank Professor A. Paul Alivisatos for use of the powder X-ray diffractometer.

Supporting Information Available: More TEM images, size distribution histograms, and FTIR spectrum of Rh nanocrystals and UV−vis spectra of $Rh(acac)_3$, PVP, and Hacac in 1,4-butanediol/ethanol solutions (PDF). This material is available free of charge via the Internet at http://pubs.acs.org.

References and Notes

(1) (a) Ahmadi, T. S.; Wang, Z. L.; Green, T. C.; Henglein A.; El-Sayed, M. A. *Science* **1996**, *272*, 1924. (b) Narayanan, R.; El-Sayed, M. A. *J. Phys. Chem. B* **2005**, *109*, 12663. (c) Launay, F.; Roucoux, A.; Patin, H. *Tetrahedron Lett.* **1998**, *39*, 1353. (d) Narayanan, R.; El-Sayed, M. A. *J. Phys. Chem. B* **2003**, *107*, 12416. (e) Thomas, J. M.; Johnson, B. F. G.; Raja, R.; Sankar, G.; Midgley, P. A. *Acc. Chem. Res.* **2003**, *36*, 20. (f) Niesz, K.; Koebel, M. M.; Somorjai, G. A. *Inorg. Chim. Acta* **2006**, *359*, 2683. (g) Rioux, R. M.; Song, H.; Grass, M.; Habas, S.; Niesz, K.; Hoefelmeyer, J. D.; Yang, P.; Somorjai, G. A. *Top. Catal.* **2006**, *39*, 167. (h) Anderson, M. L.; Stroud, R. M.; Rolison, D. R. *Nano Lett.* **2002**, *2*, 235.

(2) (a) Song, H.; Kim, F.; Connor, S.; Somorjai, G. A.; Yang, P. *J. Phys. Chem. B* **2005**, *109*, 188. (b) Song, H.; Rioux, R. M.; Hoefelmeyer, J. D.; Komor, R.; Niesz, K.; Grass, M.; Yang, P.; Somorjai, G. A. *J. Am. Chem. Soc.* **2006**, *128*, 3027.

(3) Somorjai, G. A. *Introduction to Surface Chemistry and Catalysis*; Wiley: New York, 1994.

(4) (a) Humphrey, S. M.; Grass, M. E.; Habas, S. E.; Niesz, K.; Somorjai, G. A.; Tilley, T. D. *Nano Lett.* **2007**, *7*, 785. (b) Hoefelmeyer, J. D.; Niesz, K.; Somorjai, G. A.; Tilley, T. D. *Nano Lett.* **2005**, *5*, 435. (c) Zettsu, N.; McLellan, J. M.; Wiley, B.; Yin, Y.; Li, Z.-Y.; Xia, Y. *Angew. Chem., Int. Ed.* **2006**, *45*, 1288. (d) Park, K. H.; Jang, K.; Kim, H. J.; Son, S. U. *Angew. Chem., Int. Ed.* **2007**, *46*, 1152.

(5) Stowell, C. A.; Korgel, B. A. *Nano Lett.* **2005**, *5*, 1203.

(6) (a) Xiong, Y.; McLellan, J. M.; Yin, Y.; Xia, Y. *Angew. Chem., Int. Ed.* **2007**, *46*, 790. (b) Xiong, Y.; Chen, J.; Wiley, B.; Xia, Y.; Aloni, S.; Yin, Y. *J. Am. Chem. Soc.* **2005**, *127*, 7332.

(7) (a) Chen, J.; Herricks, T.; Xia, Y. *Angew. Chem., Int. Ed.* **2005**, *44*, 2589. (b) Lee, H.; Habas, S. E.; Kweskin, S.; Butcher, D.; Somorjai, G. A.; Yang, P. *Angew. Chem., Int. Ed.* **2006**, *45*, 7824.

(8) (a) Tao, A.; Sinsermsuksakul, P.; Yang, P. *Angew. Chem., Int. Ed.* **2006**, *45*, 4597. (b) Chen, S.; Carroll, D. L. *J. Phys. Chem. B* **2004**, *108*, 5500.

(9) (a) Seo, D.; Park, J. C.; Song, H. *J. Am. Chem. Soc.* **2006**, *128*, 14863. (b) Wu, H.-Y.; Liu, M.; Huang, M. H. *J. Phys. Chem. B* **2006**, *110*, 19291.

(10) (a) Pellegatta, J.-L.; Blandy, C.; Collière, V.; Choukroun, R.; Chaudret, B.; Cheng, P.; Philippot, K. *J. Mol. Catal. A* **2002**, *178*, 55. (b) Yoon, T.-J.; Kim, J. I.; Lee, J.-K. *Inorg. Chim. Acta* **2003**, *345*, 228. (c) Halttunen, M. E.; Niemelä, M. K.; Krause, A. O. I.; Vaara, T.; Vuori, A. I. *Appl. Catal. A* **2001**, *205*, 37.

(11) (a) Narayanan, R.; El-Sayed, M. A. *Nano Lett.* **2004**, *4*, 1343. (b) Narayanan, R.; El-Sayed, M. A. *J. Am. Chem. Soc.* **2004**, *126*, 7194.

(12) Dietz, W. A. *J. Gas Chromatogr.* **1967**, *5*, 68.

(13) (a) Wang, Z. L. *J. Phys. Chem. B* **2000**, *104*, 1153. (b) Marks, L. D. *Rep. Prog. Phys.* **1994**, *57*, 603.

(14) Abe, Y.; Kato, K.; Kawamura, M.; Sasaki, K. *Surf. Sci. Spectra* **2001**, *8*, 117.

(15) Xiong, Y.; Cai, H.; Wiley, B. J.; Wang, J.; Kim, M. J.; Xia, Y. *J. Am. Chem. Soc.* **2007**, *129*, 3665.

(16) (a) Yang, P. *Nature* **2003**, *425*, 243. (b) Markovich, G.; Collier, C. P.; Henrichs, S. E.; Remacle, F.; Levine, R. D.; Heath, J. R. *Acc. Chem. Res.* **1999**, *32*, 415. (c) Collier, C. P.; Saykally, R. J.; Shiang, J. J.; Henrichs, S. E.; Heath, J. R. *Science* **1997**, *277*, 1978. (d) Kim, F.; Kwan, S.; Akana, J.; Yang, P. *J. Am. Chem. Soc.* **2001**, *123*, 4360. (e) Whang, D.; Jin, S.; Wu, Y.; Lieber, C. M. *Nano Lett.* **2003**, *3*, 1255.

(17) Dorling, T. A.; Eastlake, M. J.; Moss, R. L. *J. Catal.* **1969**, *14*, 23.

(18) Argo, A. M.; Odzak, J. F.; Goellner, J. F.; Lai, F. S.; Xiao, F. S.; Gates, B. C. *J. Phys. Chem. B* **2006**, *110*, 1775.

(19) Quinlan, M. A.; Somorjai, G. A. Structure Sensitivity Studies of Ethylene Hydrogenation on Platinum and Rhodium Surfaces. Ph.D. Thesis, University of California, Berkeley, CA, 1996.